Experimental and numerical investigation of a fluid inerter for structural control

Miriam Chillemi [a], Thomas Furtmüller [a], Christoph Adam [a,*], Antonina Pirrotta [b]

[a] *Universität Innsbruck, Unit of Applied Mechanics, Technikerstr. 13, 6020 Innsbruck, Austria*
[b] *University of Palermo, Department of Engineering, viale delle Scienze, 90128 Palermo, Italy*

ARTICLE INFO

ABSTRACT

In the study presented here, the dynamic properties of a fluid inerter, including nonlinear effects, are characterized and the degree of its effectiveness in structural control is assessed. A fluid inerter is a mechanical device that models an element with unit of mass whose mass property (called inertance) greatly exceeds its physical mass. To this end, a small-scale prototype is realized and experimentally investigated. Linear and nonlinear parameters are identified to obtain a mechanical model suitable for more accurate parametric studies. Numerical simulations based on a finite element model are performed to evaluate the effects of the air unavoidably trapped in the system. In order to apply the device to engineering problems in more general configurations, a linearization procedure is performed for the nonlinear system elements and a comparison is made between the real and the linearized system.

1. Introduction

The introduction of the so-called inerter as an alternative to the mass elements by Smith [1] marked a profound novelty in the field of mechanics of vibratory systems. Since then, this device has been continuously attracted attention in the scientific community. The concept of an ideal inerter is based on a mechanical two-terminal, one-port device whose equal and opposite resisting force F_I applied at the nodes is proportional to the relative acceleration between them [1],

$$F_I(t) = b(\ddot{x}_2(t) - \ddot{x}_1(t)) \tag{1}$$

The constant of proportionality b is called inertance and has units of kilograms, with $\ddot{x}_1$ and $\ddot{x}_2$ representing total accelerations of the two terminals.

In Eq. (1), the coefficient b represents a fictitious mass for the system to which the inerter is attached, which can be considerably larger compared to its physical mass.

Due to this property, inerters were first used in automotive engineering as an application for vibration suppression systems. Several layouts including dampers and springs were optimized for various performance criteria [2]. However, in the last 10 years, inerters have also gained attention in civil engineering and triggered a shift in the field of structural control. At the same time, the development of innovative devices that can be even more effectively reducing vibration amplitudes has been one of the most flourishing research area in recent years [3]. As a consequence, the performance of conventional vibration mitigation systems, such as Tuned Mass Dampers [4], Tuned Liquid Dampers [5], Tuned Liquid Column Dampers [6], Base Isolation Systems (BISs) [7] etc., can therefore be enhanced by the mass amplification property of inerters. For this reason, inerters, in combination with other

---

Table 1
Advantages and disadvantages of mechanical and fluid inerters.

Operating principle	Inerter type	General representation [27]	Inertance [27]	Advantages	Disadvantages
Flywheel-based	Rack-and-pinion		$b = \frac{m_0 \gamma_0^2 + m\gamma^2 \alpha^2}{r_2}$	• Large mass amplification • Strong bearing capacity [28]	• Gear backlash [29] • Inherent friction [29] • Limited layout [30]
	Ball-screw		$b = \left(\frac{2\pi\gamma}{p}\right)^2 m$	• Large mass amplification • Less friction than in rack-and-pinion inerters [26]	• Backlash [31] • Self-locking [32] • Need to be lubricated [2]
Fluid-based	Helical-tube fluid		$b = \rho l \frac{A_1^2}{A_2}$	• Large mass amplification • Flexible layout [30] • Less backlash and parasitic effects [22] • Low maintenance requirement	• Nonlinear damping [33] • Durable sealing necessary [34] • Friction [35]

r = radius of the rack pinion, m_0 = rack pinion and gear mass, γ_0 = rack pinion and gear radius of gyration, m = flywheel and pinion mass, γ = flywheel and pinion radius of gyration, α = gearing ratio, p = pitch of the screw, ρ = density of the working fluid, l = length of the external pipe, A_1 = cross-sectional area of the main cylinder minus the rod, A_2 = cross-sectional area of the external pipe.

mechanical elements, theoretically allow the realization of more effective alternatives to these devices due to the application of a lower mass to reduce accelerations in vibrations-prone structures. For example, Tuned Inerter Dampers [8], Tuned Mass Damper Inerters (TMDIs) [9], TMDIs in combination with BISs [10], Tuned Liquid Column Damper Inerters [11], Tuned Viscous Mass Dampers [12] or Rotational Inertia Double-Tuned Mass Dampers [13] are some of the applications where the inerter is exploited as an auxiliary device with the advantages of smaller size, lower physical mass, and two free terminals that can be used in linear or rotational motion. Despite these theoretical advances, applications of inerters in civil engineering practice are remain rare [14]. Therefore, the gap between the current development of vibration control systems including inerters and their application in civil engineering is far from being bridged. This is most likely due to limitations in their arrangement (especially considering that the best control is achieved when one of the two terminals is grounded [15]) as well as limitations in the mass amplification effect of heavy structures such as those encountered in the civil engineering field. Generally, physical implementations of inerters, which have been built and tested in laboratory, may be classified into two main types: flywheel-based and fluid-based. The first group includes mechanical devices such as rack-and-pinion inerters [16], in which the relative displacement of the terminals is converted into a rotation of the flywheel using a rack, pinion, and gears, and ball screw inerters [17], in which a ballscrew mechanism is employed [18]. On the other hand, fluid inerters [19] achieve the inertial effect through the working fluid flow and not through the flywheel motion. Obviously, for heavy structures such as in civil engineering, multiple flywheels should be employed for an effective mass amplification effect of the inerter. As a result of the reduced space requirement, the overall lighter and smaller arrangement of devices that do not require a flywheel makes the latter more extensively exploitable for civil engineering applications. Therefore, the absence of the flywheel can be seen as an advantage of fluid inerters, resulting in more flexible and adaptable devices. Commonly, helical-tube fluid inerters are configured as a piston with a through rod that slides inside a cylinder equipped with a helical tube and filled with a hydraulic fluid (usually water or oil). The piston moving back and forth induces the flow of the fluid through the cylinder and the helical pipe. Table 1 systematically summarizes the properties of mechanical and fluid inerters. As shown, the different characteristics of these devices, in addition to the differences in their operating principles and physical realizations, lead to a series of advantages and disadvantages intrinsically linked to their nature. Specifically, a large mass amplification effect can be obtained in all cases. However, fluid inerters result in a design that may be considered more suitable for civil engineering applications, as they can be used in a variety of damper arrangements [20], while preserving a magnification effect of up to 10,000 times the fluid mass itself [21]. Moreover, parasitic effects such as backlash and ratcheting, which strongly affect the mechanical alternatives, appear to be less pronounced in fluid inerters [22]. Apart from the advantages they provide, other contributions, such as pronounced nonlinear damping effects and friction, may be important, and their impact are still unclear. While mechanical inerters have been widely analyzed experimentally [23–26], experiments with fluid inerters and analyses on their control performance have not yet been studied in depth.

In a previous study [35], a fluid inerter prototype was experimentally tested and its parameter numerically identified. In this case, the model was developed with only one design parameter setting. However, since the inertance is mainly influenced by physical and geometrical considerations (see equations in Table 1), changing one of the design parameter, for example, the external tube length, would help to prove the reliability of the theoretical understanding of a fluid inerter. For this reason, in the present work, the inerter prototype is investigated in a different design to accurately determine its physical properties and characterize its nonlinearities. Indeed, the assumption of a linear behavior for this type of devices may lead to oversimplified models and therefore to an incorrect assessment of their control performance [31]. However, the increasing complexity of the mechanical model results in cumbersome computations that are unsuitable for the development of further dynamic simulations of inerter-based devices. With this in mind,
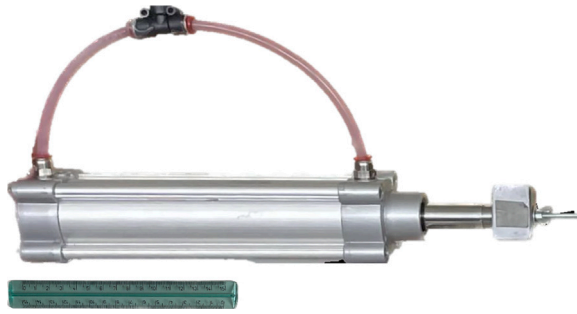
Fig. 1. Small-scale prototype of the fluid inerter.

this study proposes a linearization procedure that allows feasible numerical analyses while preserving the real behavior of the fluid inerter. This includes also simulations that can finally investigate difficult-to-analyze aspects of the device performance. In particular, in the present work, for the first time, a finite element analysis of the fluid inerter is developed and used to assess the influence of the air trapped in the device. Indeed, for the achievement of a very close to reality model, it seemed necessary to consider the unintended presence of a certain amount of air in the system, even in the case of extreme caution during testing [36]. Another potential cause for this undesired effect could be the occurrence of cavitation phenomena, which have already detected in previous studies [37] but have not been studied in depth. Finally, the present study not only merely analyzes the linear and nonlinear characteristics of a fluid inerter itself, but also evaluates its properties in terms of structural control. In fact, the device is also investigated experimentally when it is coupled to a system whose vibrations must be mitigated. This type of application makes it possible to realistically demonstrate the potential of a real inerter when applied for structural control in addition to the ideal numerical simulations already extensively conducted.

The paper is organized as follows: Section 2 describes the experimental setup and presents the results of the experiments. In Section 3, suitable mechanical models are developed for the different configurations considered and the parameters of these models are identified, contrasting the outcomes with the experimental data. In Section 4, the linearization of the nonlinear elements in the model is performed and the results of the linearized systems are shown. Finally, Section 5 includes the simulation based on a finite element model of the device developed to evaluate the effect of air in the system.

2. Experimental setup

2.1. Prototype design

Fig. 1 shows the small-scale prototype of a fluid inerter developed at the Unit of Applied Mechanics, Universität Innsbruck. The prototype consists of a hydraulic cylinder in which a piston moves back and forth. The piston head divides the cylinder into two chambers and is equipped with sliding rings and rubber seals to prevent flow between the two parts. The cylinder barrel is closed at one end by the cylinder bottom and rigidly connected to an IPE steel profile that serves as a clamping. The other terminal is linked to an electro-dynamic shaker that provides the input force. Water is chosen as the working medium due to its properties and ease of use and availability. The inertia effect therefore results from the flow in the external channel, which is attached to the cylinder by means of two watertight valves. The properties of the prototype described above are listed and graphically summarized in Table 2. Employing the equation reported in Table 1 for a fluid inerter, the inertance is predicted to be $b = 29$ kg, while the actual mass of the device including cylinder, piston, and external pipe is less than 2 kg and the mass of the working fluid is only about 300 g.

2.2. Experimental test procedure

With the aim of identifying the dynamic properties the fluid inerter device (FID) and assessing its performance when employed as vibration control system, four different tests are performed. The first step is to identify the uncontrolled system (US) (Fig. 2 - US), i.e. the structure whose vibrations are to be mitigated by the device. It consists of a single degree-of-freedom (DOF) system with a block of mass $m_s = 27$ kg rigidly attached to a sliding table of dimensions 30×30 cm, while compression springs are used to tune the natural frequency of the system. Second, the inerter without the presence of the working fluid, referred to as the dry inerter device (DID), is examined (Fig. 2 - DID). This type of test was deemed necessary in previous studies [35] because hydraulic systems such as hydraulic cylinders require accurate consideration of friction in the model employed [38]. It is obvious that its understanding is facilitated when other effects related to the presence of the working fluid are not present. After characterizing the tribological behavior of the piston rod sliding through the cylinder, the inertial properties of the system filled with water, referred to as fluid inerter device (FID), are identified (Fig. 2 - FID). The last experiment, shown in Fig. 2 - CS, concerns the controlled system (CS), where the main system is controlled by the FID.

In all four steps, the system is dynamically excited by an APS 400 Electro-Seis long-stroke shaker from APS Dynamics, Inc., driven by an APS 145 power amplifier. The force is measured with an impedance head of type AF/100/10 from DJB Instruments.

Table 2
Parameters and sketch of the small-scale prototype.

Parameter	Symbol	Value
Stroke length [mm]	L_c	200
Cylinder Ø [mm]	D_c	5
Piston rod Ø [mm]	D_p	20
Piston mass [kg]	m_p	0.925
Area of the cylinder minus the rod [m²]	A_1	1.64×10^{-3}
External pipe Ø [mm]	D_h	6
External pipe length [m]	l_h	0.3
Area of external pipe [m²]	A_2	0.028×10^{-3}
Working fluid density [kg m⁻³]	ρ_l	995.6
Working fluid bulk modulus [Pa]	B_l	2.1×10^9
Working fluid mass [kg]	m_l	0.338
Inertance [kg]	b	29
Cylinder barrel material	–	Anodized aluminum
Cylinder heads material	–	Die-cast aluminum
Piston material	–	Chromed steel
Seals material	–	Nitrile rubber
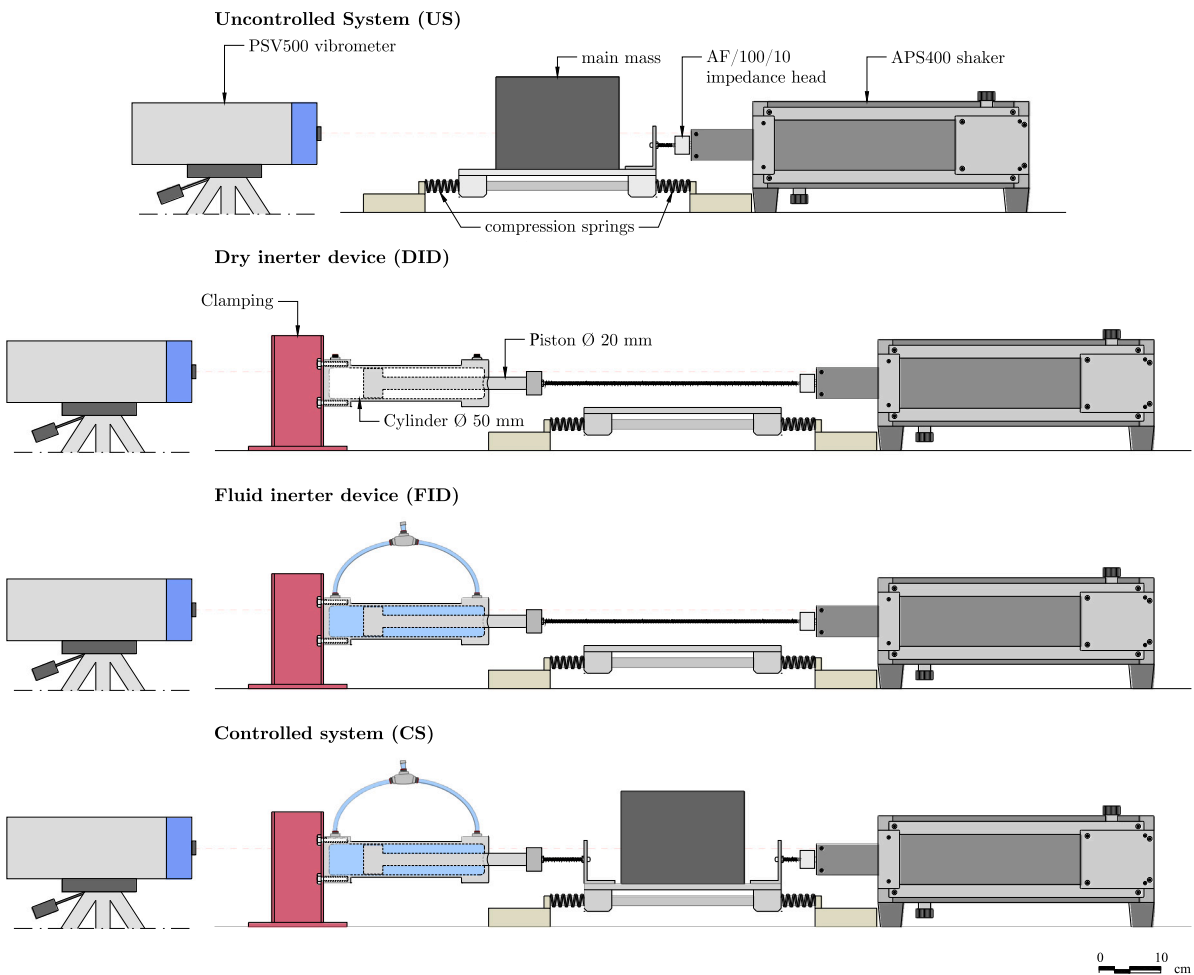
Fig. 2. Schematic of the four experimentally tested configurations.

The velocity of the piston is recorded by a laser vibrometer of type PSV500 from Polytec, from which the displacement magnitude in the frequency domain is subsequently determined. A linear sweep (chirp) in the frequency range from 1 to 10 Hz in a period of 60 s with constant voltage amplitude is used as the excitation signal for the power amplifier.
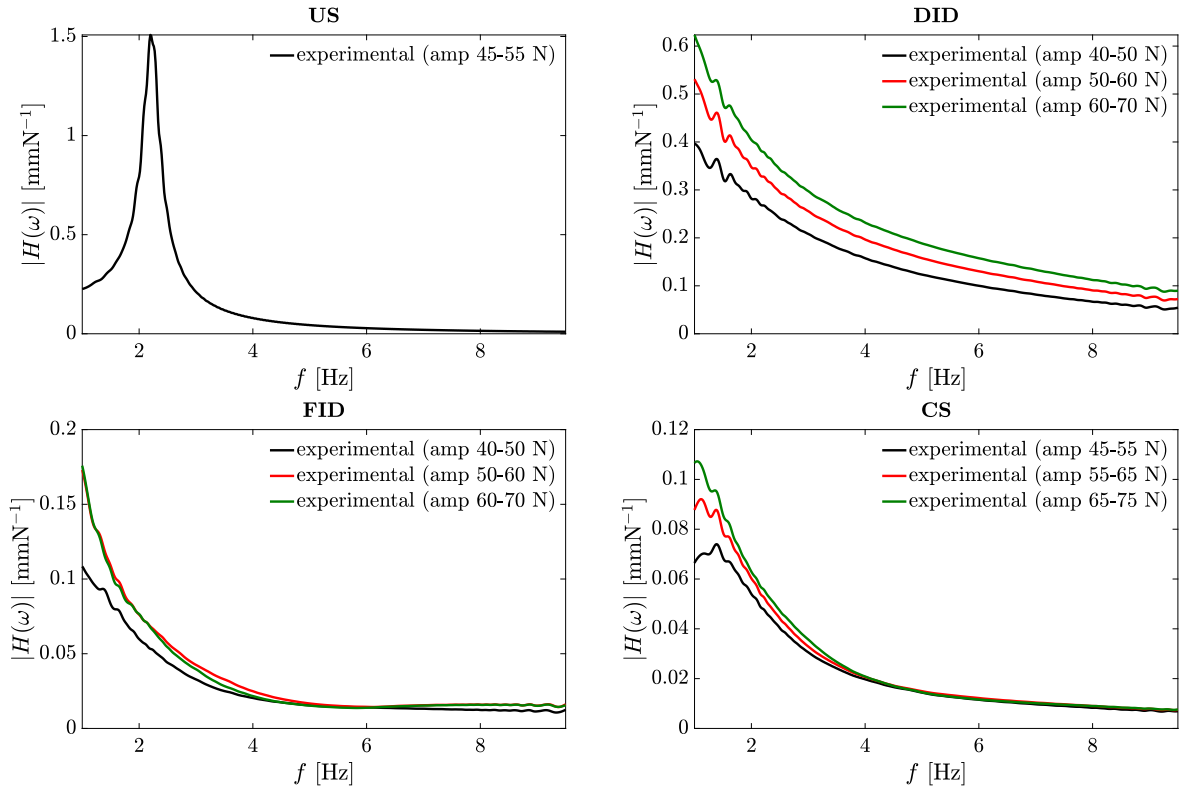
Fig. 3. Experimental results in terms of receptance of uncontrolled system (US), dry inerter device (DID), fluid inerter device (FID), and controlled system (CS) for different excitation signal amplitudes.

2.3. Experimental outcomes

As a result of the experiments, Fig. 3 shows the receptance magnitude $|H(\omega)|$ (i.e., the ratio of displacement over input force in frequency domain) for each test. For US (top left subplot), the result refers to the displacement of the mass m_s itself, while for DID, FID and CS the displacement of the piston is considered. In order to reveal nonlinear effects, different excitation amplitudes are applied to the latter experiments, changing the magnitude of the input voltage. Since the applied input voltage is constant, the resulting exciting force amplitude is not constant due to the interaction of the shaker with the devices under test. Therefore, the input force amplitudes given in Fig. 3 are not single values but 10 N ranges. From the top left subplot, a natural frequency $f_s = 2.3$ Hz and a damping ratio $\zeta_s = 0.02$ can be deduced for the uncontrolled system, employing the receptance for a linear single DOF oscillator. As can be seen in DID (top right subplot), as the amplitude of the input signals increases, the amplitudes of $|H(\omega)|$ increase, indicating a nonlinear effect due to friction between the piston rod and cylinder. In contrast, the nonlinear behavior is less pronounced for FID (bottom right subplot) and CS (bottom left subplot) and is only noticeable for low frequencies.

3. Numerical simulations

To numerically reproduce the experimental results and reveal nonlinear effects, mechanical models are developed for the four configurations considered in Section 2.2 and shown in Fig. 4. In previous studies [35], it has been shown to be beneficial to include the vibration exciter in the simulation models. Although the force measured by the impedance head could be used as input for the numerical simulations, the necessary interpolation between the recorded samples in the numerical time integration scheme would make the simulations rather time consuming. On the other hand, considering an electromechanical system for the shaker, the same voltage signal can be used as in the experimental studies. In the particular case of the linear sweep used, this signal is available as a function of time, hence no interpolation is required. Following [39], the electro-dynamic shaker is modeled as a two DOF system, with shaker displacement $x_1(t)$ of the shaker mass m_a and the electrical current $i(t)$ as DOFs. The lumped mass m_a is connected to the ground via a connecting element C_a, which consists of a Kelvin–Voigt component with spring stiffness k_a and damping coefficient c_a and represents the mechanical part of the shaker, while R and L are the resistance and the inductance of the shaker coil, respectively. The four mechanical systems are excited by a force F proportional to the current and the electrical circuit is additionally excited by an internal voltage proportional to the velocity of the coil. The constants of proportionality are denoted by α_1 and α_2, while $u(t)$ is the input voltage.
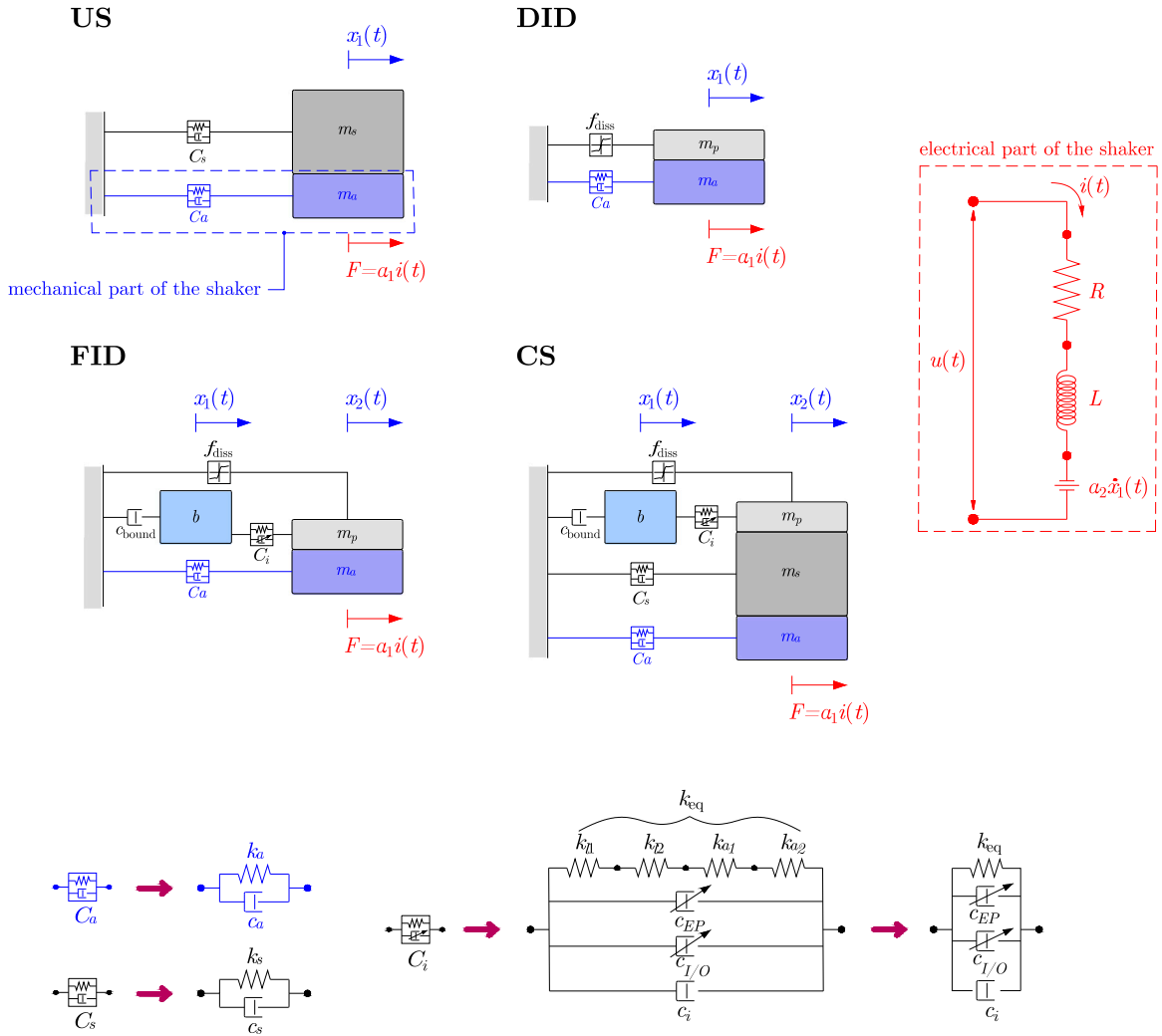
Fig. 4. Electro-mechanical models of uncontrolled system (US), dry inerter device (DID), fluid inerter device (FID), and controlled system (CS).

Generally, the equations of motion of the systems shown in Fig. 4 can be written as

$$\mathbf{M}\,\ddot{\mathbf{x}} + \mathbf{C}\,\dot{\mathbf{x}} + \mathbf{K}\mathbf{x} = \mathbf{f} \tag{2}$$

where a dot over a variable stands for derivation with respect to time. The matrices $\mathbf{M}$, $\mathbf{C}$, $\mathbf{K}$ and the vectors $\mathbf{x}$ and $\mathbf{f}$ will be defined in the following for each configuration.

3.1. Uncontrolled system

In the US shown schematically in Fig. 4 - US, the main mass m_s is rigidly attached to the terminal of the shaker, i.e. to the mass m_a, on one side and grounded via the connecting element C_s on the other side. This consists of a spring–dashpot element of stiffness k_s and damping c_s. The US, thus, exhibits two DOFs, the displacement $x_1(t)$ and the current $i(t)$. However, considering $i(t)$ as the electric DOF, the matrix $\mathbf{M}$ would contain zero elements on the main diagonal. As a result, standard ODE solvers cannot be used to compute the response of Eq. (2) since the inverse matrix $\mathbf{M}^{-1}$ cannot be computed. To avoid poor computational efficiency by using implicit ODE solvers, the electric charge q is employed as the electrical quantity instead of the current i. By applying the relations [40]

$$\dot{q}(t) = i(t) \;,\quad \ddot{q}(t) = \frac{di}{dt} \tag{3}$$

the matrices $\mathbf{M}$, $\mathbf{C}$, $\mathbf{K}$ and the vectors $\mathbf{x}$ and $\mathbf{f}$ in Eqs. (2) now read

$$\mathbf{M} = \begin{bmatrix} m_a + m_s & 0 \\ 0 & L \end{bmatrix} \;,\quad \mathbf{C} = \begin{bmatrix} c_a + c_s & -\alpha_1 \\ \alpha_2 & R \end{bmatrix} \;,\quad \mathbf{K} = \begin{bmatrix} k_a + k_s & 0 \\ 0 & 0 \end{bmatrix} \;,$$

$$\mathbf{x} = \begin{Bmatrix} x_1(t) \\ q(t) \end{Bmatrix} \quad , \quad \mathbf{f} = \begin{Bmatrix} 0 \\ u(t) \end{Bmatrix} \tag{4}$$

In this way, the system of Eqs (2) can be reformulated as first-order system and can be solved, for instance, in MATLAB by the standard *ode45* solver. Table 3 summarizes the parameters included in Eq. (4), noting that the electromechanical properties of the shaker (R, L, k_a, c_a, α_1 and α_2) are known from previous studies [35].

3.2. Dry inerter device

The mechanical model of the DID is shown in Fig. 4 - DID. In this case, the piston mass m_p is rigidly connected to the shaker mass m_a and its displacement $x_1(t)$ corresponds to the mechanical DOF of the system. To model the friction between the piston rod and cylinder, a dissipation force element f_{diss} is introduced [41]. Based on previous studies [35], f_{diss} is assumed to be a function of velocity $\dot{x}_1$, since simpler models such as Coulomb friction without velocity dependence failed in modeling the friction of the system due to a pronounced stick–slip phenomenon. In contrast, the so-called Stribeck effect [42] captures the friction behavior more accurately, resulting in a larger force at or near zero velocity and smaller force at high velocities. This nonlinear effect can be viewed as a combination of three different forces: static friction (or stiction) F_s, dynamic friction (or Coulombic friction) F_d, and viscous force due to contacts between lubricated surfaces. Hence, the friction behavior of the system can be modeled as [43]:

$$f_{\text{diss}}(\dot{x}_1) = \left(F_d \tanh\left(4\frac{|\dot{x}_1|}{v_s}\right) + (F_s - F_d)\frac{\frac{|\dot{x}_1|}{v_s}}{\left(\frac{1}{4}\left(\frac{|\dot{x}_1|}{v_s}\right)^2 + \frac{3}{4}\right)^2} \right) \text{sgn}(\dot{x}_1) + r\dot{x}_1 \tag{5}$$

where v_s is the so-called Stribeck velocity and corresponds to the velocity value that occurs when the maximum static friction is encountered and r is the viscous damping coefficient. Thus, for the DID, the matrices $\mathbf{M}$, $\mathbf{C}$, $\mathbf{K}$ and the vectors $\mathbf{x}$ and $\mathbf{f}$ in Eqs. (2) can be written as

$$\mathbf{M} = \begin{bmatrix} m_a + m_p & 0 \\ 0 & L \end{bmatrix} \quad , \quad \mathbf{C} = \begin{bmatrix} c_a & -\alpha_1 \\ \alpha_2 & R \end{bmatrix} \quad , \quad \mathbf{K} = \begin{bmatrix} k_a & 0 \\ 0 & 0 \end{bmatrix} \quad ,$$
$$\mathbf{x} = \begin{Bmatrix} x_1(t) \\ q(t) \end{Bmatrix} \quad , \quad \mathbf{f} = \begin{Bmatrix} -f_{\text{diss}}(\dot{x}_1) \\ u(t) \end{Bmatrix} \tag{6}$$

The unknown values are identified by numerical simulations and optimization with respect to the experimental outcomes presented in Section 2.3. The *GlobalSearch* function implemented in MATLAB is used, employing the *fmincon* optimization algorithm. As objective function the sum of the squared error between the experimental and numerical receptances was employed in the entire frequency range and for all different amplitudes. The parameters obtained are listed in Table 3. Fig. 5 compares the receptance magnitudes for three input amplitudes ranges. Solid black lines refer to the experimental results and dashed red lines show the numerical results. The comparison demonstrates that results of experiment and simulation are in good agreement. However, more significant deviations at lower frequencies underscore the significant influence of the friction on the DID. Clearly, the friction model adopted, although more sophisticated than pure Coulomb friction, is still a simplification with respect to the somewhat stochastic nature of the friction observed in the tests. Nevertheless, as it will be shown later, the limitations in terms of accuracy of the dissipation force of Eq. (5) do not affect the results for the system in wet conditions as much.

3.3. Fluid inerter device

Fig. 4 - FID shows the mechanical model of the FID. Here, the mass b is introduced, which models the effect of inertial mass due to water flow in the external pipe by an additional DOF. Thus, in addition to the electrical DOF $q(t)$, the two mechanical DOFs are $x_1(t)$ and $x_2(t)$, corresponding respectively to the relative displacement of the piston mass and the water inertance with respect to the ground. The inertial mass b is grounded by means of the dash-pot damper c_{bound}, which models the effects of boundary conditions such as the movements to which the external pipe is subjected during the test, and connected to the piston m_p on the other side via the connector element C_i. The latter models the compressibility of the fluid as well as the behavior of the air trapped in the system by a series of springs arranged in parallel to the dash-pot dampers. Although care was taken during the experiments to prevent air infiltration in the system, this undesirable effect is unavoidable [36]. Furthermore, air in the system may be due to the formation of air bubbles at a later stage than the test rig preparation as a result of cavitation [37]. This refers to the formation of air in a fluid as its absolute pressure approximates that of saturated vapor at the temperature of water. While this effect is represented by linear elastic springs in the mechanical model presented, a more detailed investigation of the influence of air employing finite element simulations is reported in Section 5.

The spring k_{eq} of the connector element C_i is the sum of the reciprocal values of the series of springs modeling the behavior of air and fluid. The following relationship is used to characterize the equivalent air spring stiffnesses k_{aj},

$$k_{aj} = \gamma \, A_j^2 \frac{p_0}{V_0}\left[1 - \frac{A_j}{V_0}(x_2 - x_1)\right]^{-(\gamma+1)} \tag{7}$$

which was originally introduced to model this effect in Tuned Liquid Column Dampers (TLCD) [44].
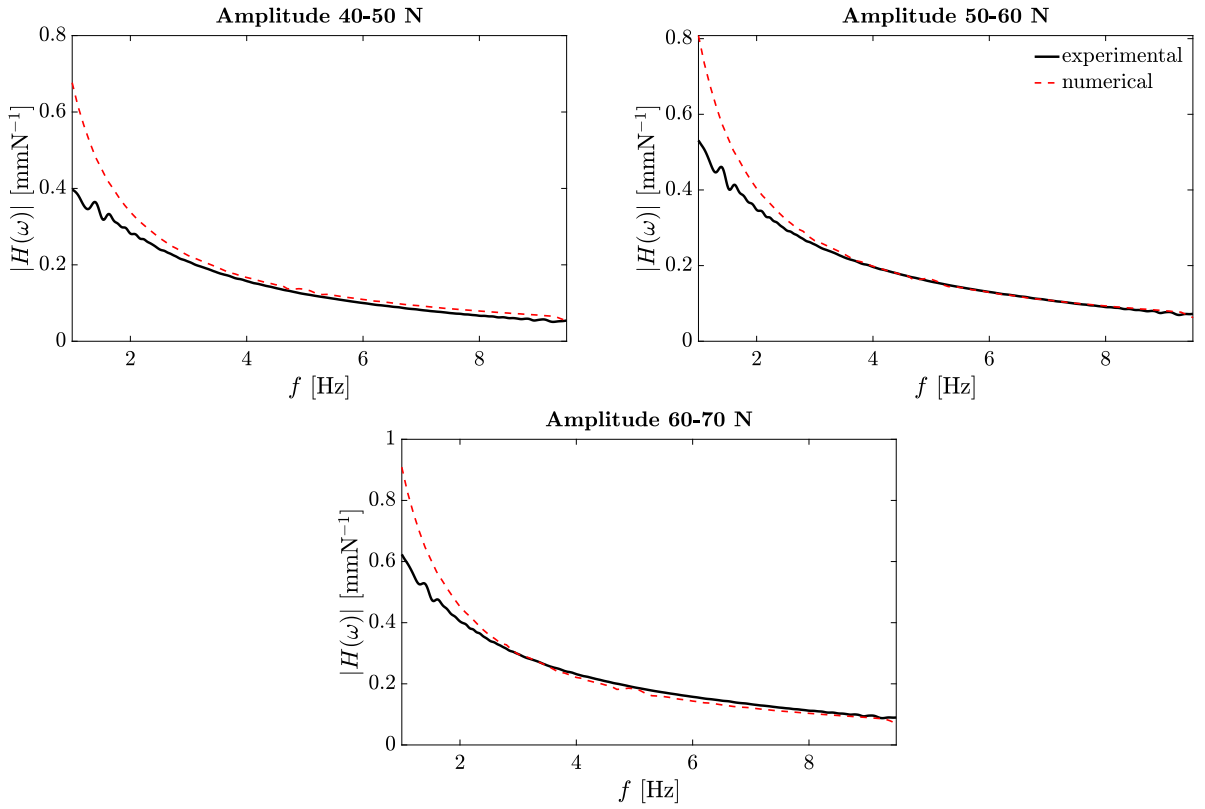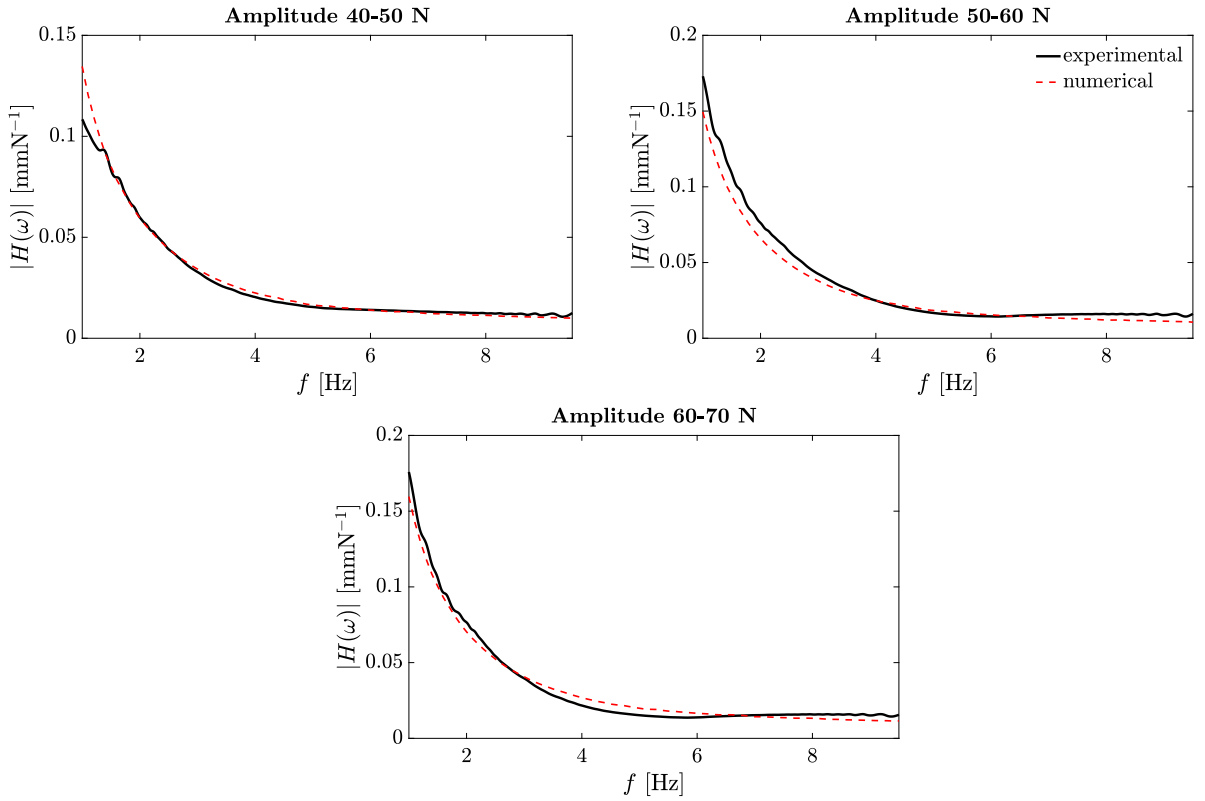
Fig. 5. Experimental (solid black line) versus numerical (dashed red line) receptance response of the dry inerter device.

In Eq. (7), $j = 1, 2$ denotes the cylinder and the external pipe geometry, respectively, p_0 the atmospheric pressure, V_0 the volume of the air column, and $\gamma = 1.4$ the specific heat ratio. The equivalent spring stiffnesses of the water, k_{lj} take into consideration that system components containing compressible fluid exhibit the behavior of a spring in determining the dynamics of the system. This stiffness can be viewed as the ratio of the volume decrease due to an increase in pressure and is given by the bulk modulus of elasticity. Assuming that the bulk modulus of the working fluid B_l is constant, the stiffness of a hydraulic actuator is determined as [45]

$$k_{lj} = B_l \frac{A_j^2}{V_j} \tag{8}$$

with $j = 1, 2$ indicating the cylinder and the external pipe geometry, respectively.

In addition, dissipative effects need to be taken into account. More specifically, the viscosity of the fluid that generates pressure losses in the external pipe F_{EP}, and the inlet and outlet forces $F_{I/O}$ due to the transition of the fluid from the cylinder to the outer tube and vice-versa. Their expressions are [34,37]

$$F_{EP} = c_{EP}(\dot{x}_2 - \dot{x}_1)^{1.75} \tag{9}$$

$$F_{I/O} = c_{I/O}(\dot{x}_2 - \dot{x}_1)\left|\dot{x}_2 - \dot{x}_1\right| \tag{10}$$

$$c_{\text{inlet}} = 0.25 A_1 \rho_l \left(\frac{A_1}{A_2}\right)^2 \;, \quad c_{\text{outlet}} = 0.5 A_1 \rho_l \left(\frac{A_1}{A_2}\right)^2 \;, \quad c_{I/O} = 0.75 A_1 \rho_l \left(\frac{A_1}{A_2}\right)^2 \tag{11}$$

and

$$c_{EP} = \frac{0.0664 \mu^{0.25} \rho_l^{0.75} 0.3 A_1}{d^{1.25}} \left(\frac{A_1}{A_2}\right)^{1.75} \tag{12}$$

It should be noted that Eqs. (11) and (12) are valid for steady flow. However, the real hydraulic behavior of the fluid inside the device is unsteady, and laminar and turbulent regimes continuously alternate. Thus, Eqs. (11) and (12) are merely empirical formulas that approximate the system hydraulics as closely as possible. Nevertheless, these damping contributions, together with the dissipation force mentioned earlier, cause deviations from the ideal inerter representation and cannot be neglected since they are an intrinsic

Fig. 6. Experimental (solid black line) versus numerical (dashed red line) receptance response of the fluid inerter device.

part of the fluid inerter working mechanism. Moreover, an additional viscous damping effect is revealed and accounted for as c_i, which models dissipative effects introduced by the air. For the FID, the matrices $\mathbf{M}$, $\mathbf{C}$, $\mathbf{K}$ and the vectors $\mathbf{x}$ and $\mathbf{f}$ are defined as

$$\mathbf{M} = \begin{bmatrix} m_a + m_p & 0 & 0 \\ 0 & b & 0 \\ 0 & 0 & L \end{bmatrix}, \quad \mathbf{C} = \begin{bmatrix} c_a + c_i & -c_i & -\alpha_1 \\ -c_i & -c_i + c_{\text{bound}} & 0 \\ \alpha_2 & 0 & R \end{bmatrix}, \quad \mathbf{K} = \begin{bmatrix} k_a + k_{\text{eq}} & -k_{\text{eq}} & 0 \\ -k_{\text{eq}} & k_{\text{eq}} & 0 \\ 0 & 0 & 0 \end{bmatrix},$$

$$\mathbf{x} = \begin{Bmatrix} x_1(t) \\ x_2(t) \\ q(t) \end{Bmatrix}, \quad \mathbf{f} = \begin{Bmatrix} -f_{\text{diss}}(\dot{x}_1) - F_{EP}(\dot{x}_2 - \dot{x}_1) - F_{I/O}(\dot{x}_2 - \dot{x}_1) \\ -F_{EP}(\dot{x}_2 - \dot{x}_1) - F_{I/O}(\dot{x}_2 - \dot{x}_1) \\ u(t) \end{Bmatrix} \tag{13}$$

Since previously determined parameters characterizing the DID remain unchanged, k_{a1}, k_{a2}, c_i and c_{bound} are the only remaining free parameters. They are obtained employing the same optimization procedure as for the DID and yield values as reported in Table 3. The numerically obtained receptance magnitudes, based on the system of Eq. (13), are plotted in Fig. 6 as dashed red lines for the three different experimentally investigated input amplitudes ranges and compared with the experimental outcomes from Fig. 3 - FID. As can be seen, the agreement is very close and only minor deviations are observed in the frequency range below 3 Hz in the case of 50–60 N amplitude. This remarkable result confirms the suitability of the parameters employed (Table 3) and the correctness of the inertance value calculated theoretically.

3.4. Controlled system

Fig. 4 - FID finally shows the mechanical model of the system controlled by the FID. It still consists of three DOFs, since the mass m_s to be controlled is rigidly connected to the piston mass m_p and the shaker mass m_a. Thus, the two mechanical DOFs are $x_1(t)$ and $x_2(t)$, which correspond to the displacement of the main mass m_s and the inertial mass b and with respect to the ground. The matrices $\mathbf{M}$, $\mathbf{C}$, $\mathbf{K}$ and the vectors $\mathbf{x}$ and $\mathbf{f}$ of Eqs. (2) can be formulated as

$$\mathbf{M} = \begin{bmatrix} m_a + m_p + m_s & 0 & 0 \\ 0 & b & 0 \\ 0 & 0 & L \end{bmatrix}, \quad \mathbf{C} = \begin{bmatrix} c_a + c_s + c_i & -c_i & -\alpha_1 \\ -c_i & -c_i + c_{\text{bound}} & 0 \\ \alpha_2 & 0 & R \end{bmatrix}, \quad \mathbf{K} = \begin{bmatrix} k_a + k_s + k_{\text{eq}} & -k_{\text{eq}} & 0 \\ -k_{\text{eq}} & k_{\text{eq}} & 0 \\ 0 & 0 & 0 \end{bmatrix},$$
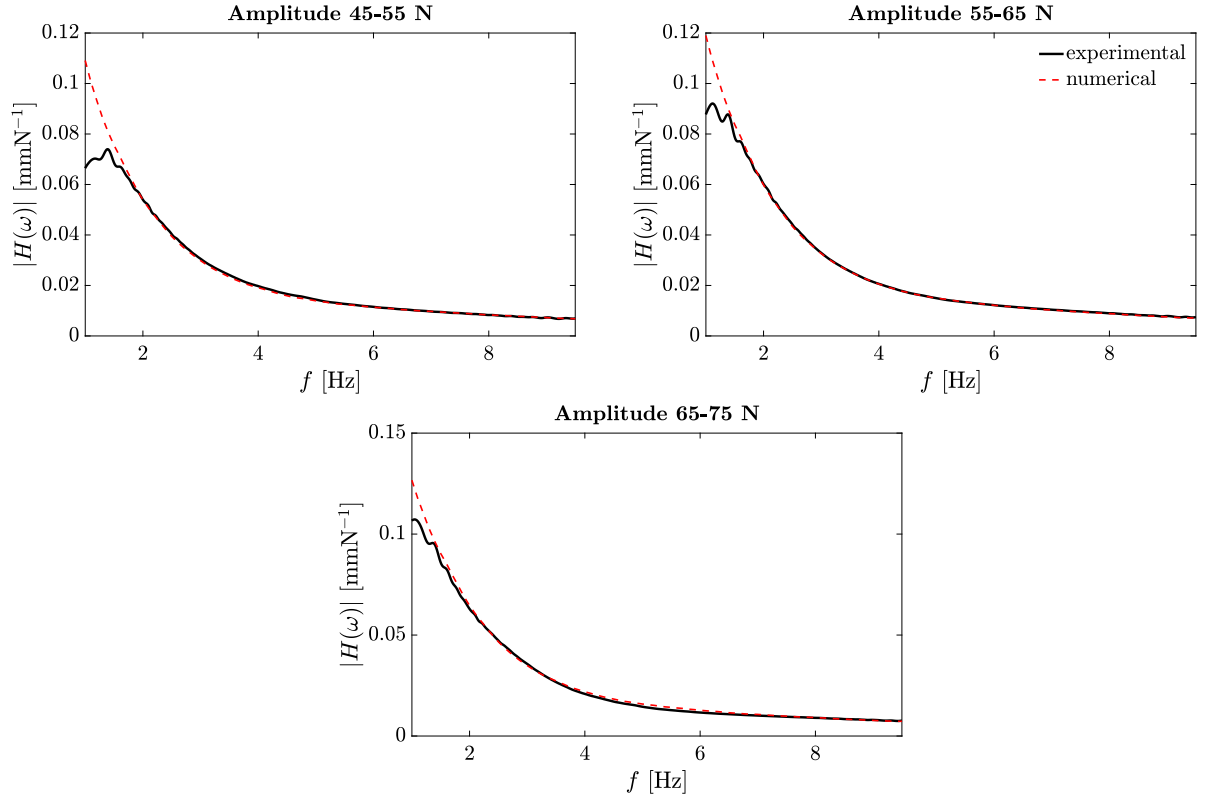
Fig. 7. Experimental (solid black line) versus numerical (dashed red line) receptance response of the controlled system.

Table 3
Parameters of the mechanical models.

Parameter	Symbol	Value	Parameter	Symbol	Value
DC Coil Resistance [Ω]	R	1.75	Static friction force [N]	F_s	21.14
Inductance [H]	L	0.022	Dynamic friction force [N]	F_d	15.07
Force–current ratio [N/A]	α_1	20	Stribeck velocity [m/s]	v_s	0.0362
Voltage–velocity ratio [V ms^{-1}]	α_2	20	Viscous damping coefficient [N s/m]	r	104.5
Armature assembly mass [kg]	m_a	2.7	Equivalent spring stiffness [N/m]	k_{eq}	3.6×10^4
Shaker stiffness [N m^{-1}]	k_a	106.59	Ext. pipe damping coefficient [N s/m]	c_{EP}	1.82×10^3
Shaker damping coefficient [N s m^{-1}]	c_a	6.79	Inlet/outlet damping coefficient [N s/m]	$c_{I/O}$	4.21×10^3
Main mass [kg]	m_s	27	Fluid damping coefficient [N s/m]	c_i	447.65
Main mass stiffness [N m^{-1}]	k_s	5.7×10^3	Boundary damping coefficient [N s/m]	c_{bound}	652.18
Main mass damping coefficient [N s m^{-1}]	c_s	15.78			

$$\mathbf{x} = \begin{Bmatrix} x_1(t) \\ x_2(t) \\ q(t) \end{Bmatrix}, \quad \mathbf{f} = \begin{Bmatrix} -f_{\text{diss}}(\dot{x}_1) - F_{EP}(\dot{x}_2 - \dot{x}_1) - F_{I/O}(\dot{x}_2 - \dot{x}_1) \\ -F_{EP}(\dot{x}_2 - \dot{x}_1) - F_{I/O}(\dot{x}_2 - \dot{x}_1) \\ u(t) \end{Bmatrix} \tag{14}$$

As can be seen in Fig. 7, the agreement between the analytical (dashed red lines) and experimental (solid black lines) receptance magnitudes is excellent. Small deviations are observed in the frequency range below 2 Hz for the lower excitation amplitudes. Since this behavior is similar to the outcomes observed for the DID, it can be concluded that the discrepancy is mainly caused by the friction model.

To illustrate the performance of the inerter as a passive vibration control device, another comparison is shown in Fig. 8. Both the experimental (solid lines) and numerical (solid lines with markers) receptance responses of the US and CS are displayed. A significant reduction in the receptance magnitude is observed throughout the frequency range, corresponding to the realized inertance-to-mass ratio $b/(m_a + m_s) \approx 1$.
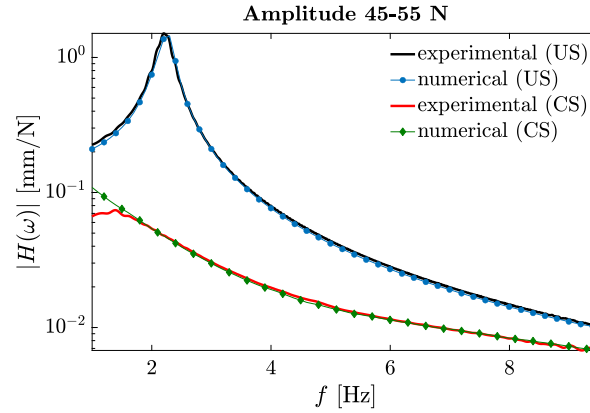
Fig. 8. Experimental (solid black line) and numerical (solid blue line with markers) receptance response of the uncontrolled system versus experimental (solid red line) and numerical (solid green line with markers) receptance response of the controlled system. (For interpretation of the references to color in this figure legend, the reader is referred to the web version of this article.)

4. Linearization

As outlined in the previous section, the friction force as well as the pressure losses in the external pipe and at the inlet and outlet are sources of nonlinearity in the inerter model. Although linear dynamic simulations are preferable and would allow the development of extended parametric studies, omitting these quantities would result in an inadequate definition of the FID since they are part of the hydraulic mechanism of the device itself. In addition, an accurate mechanical model capable of capturing the real behavior of the system would allow the need for experimental tests. As a consequence, an equivalent linear model would be the most convenient scenario to better exploit the device for analytical analyses while leaving the prediction accuracy of the model unchanged.

With the aim of linearizing the nonlinear mechanical model of the FID, energy considerations are taken into account. Conveniently, it is possible to characterize damping mechanisms as [46]:

$$F_{\text{damp}}(t) = -r\,|g(t)|\,\text{sgn}(v) \tag{15}$$

where F_{damp} is the damping force, r is a scalar damping coefficient, $|g(t)|$ is some arbitrary magnitude function. Assuming a sinusoidal displacement with x_0 as initial displacement and $\omega = 2\pi f$ as displacement circular frequency, if $g(t) = \dot{x}(t) = v(t) = x_0\omega\cos(\omega t)$, the resulting damping force has a cosine shape. The hysteresis curve of such a force consists of an ellipse with an area of $A = \omega\pi r x_0^2$ and units of energy loss per cycle. Similarly, for any damping force $F_{\text{damp}}(t)$, the energy loss per cycle can be computed as the integral of the force times the displacement, i.e. the work done per each cycle ΔE. Comparing ΔE and A, the equivalent damping coefficient r_{eq} is given by

$$r_{\text{eq}} = \frac{\Delta E}{x_0^2\omega\pi} \tag{16}$$

Eq. (16) is applied to the three nonlinear damping forces of the FID system when excited by a chirp function. In order to obtain more general expressions for the equivalent damping, purely mechanical models as depicted in Fig. 11 are considered in this section, i.e. without electrical part of the shaker. Thus, the excitation signals are forces $F(t)$ applied at the piston mass, where the amplitude of the chirp signal is constant. For the dissipation force f_{diss} caused by friction, the displacement of the piston $x_1(t)$ is considered, while for damping forces of external pipe and inlet/outlet, the relative displacement between the inertial mass b and the piston, $x_2(t) - x_1(t)$, is considered. Since these displacements computed during a sine sweep are frequency dependent, r_{eq} is obtained as a function of ω. To this end, the envelopes of the displacements $x_1(t)$ and $x_2(t) - x_1(t)$ are computed, from which the frequency-dependent amplitude $x_0(\omega)$ is readily obtained. The corresponding dissipation forces $F_d(t)$ are obtained by evaluating Eq. (5), Eq. (9), and Eq. (10), respectively. The hysteresis loops of these forces are shown in Fig. 9 for different excitation amplitudes and frequencies $f = \omega/2\pi$. Considering the dissipation force F_{diss} due to friction of the piston (first column), as the force amplitude increases, the energy loss per cycle increases, with the shape of the hysteresis curve approaching a rectangle, i.e. the shape for pure Coulomb friction. Hence, for larger force amplitudes, the dissipation force F_{diss} tends to the classic Coulomb friction behavior. As the frequencies increases, the velocity $\dot{x}_1$ increases while the displacement x_1 decreases, and more viscous behavior is obtained, i.e., a more elliptical hysteresis curve. The opposite behavior is encountered for F_{EP} and $F_{I/O}$ (second and third column, respectively). The larger is the frequency considered, the larger is the area of the hysteresis curve, i.e. the dissipated energy.

Eqs. (2) can be written in frequency domain as

$$\left(-\omega^2 \underline{\mathbf{M}} + i\omega\underline{\mathbf{C}} + \underline{\mathbf{K}}\right)\mathbf{X}(\omega) = \mathbf{F}(\omega) \tag{17}$$
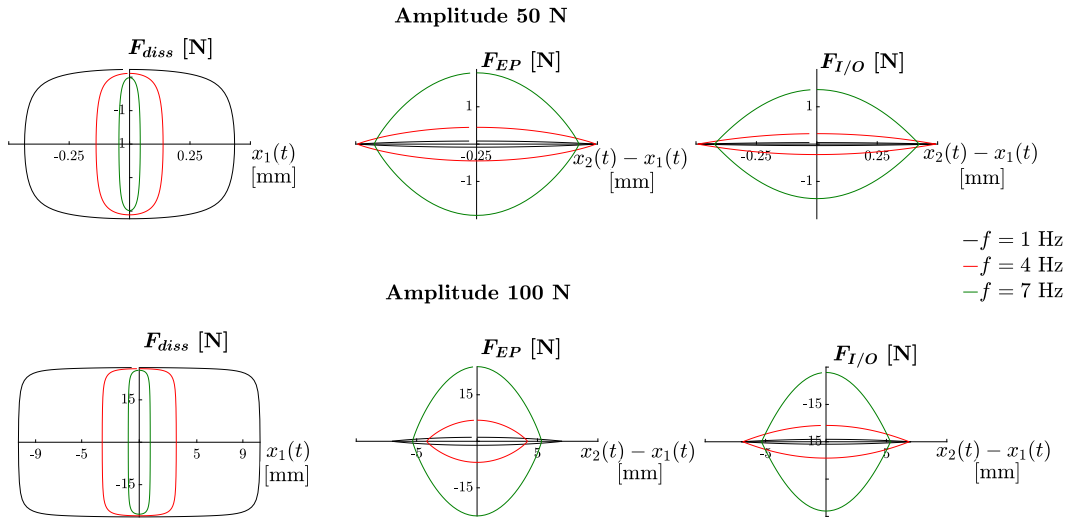
Amplitude 50 N

Amplitude 100 N

Fig. 9. Hysteresis curves of F_{diss}, F_{EP} and $F_{I/O}$ for different input amplitudes and frequencies.
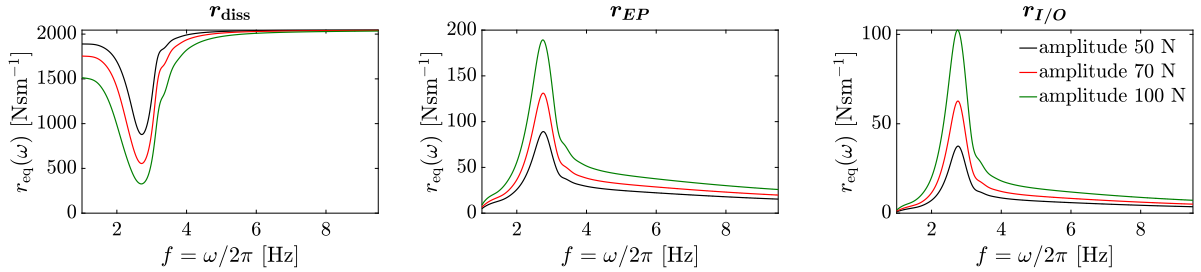

Fig. 10. Frequency dependent equivalent damping functions for different input amplitudes (solid black lines — amplitude 50 N, solid red lines — amplitude 70 N, solid green lines — amplitude 100 N. (For interpretation of the references to color in this figure legend, the reader is referred to the web version of this article.)

Here, the damping matrix $\underset{\sim}{C}$ can be considered as the sum of the linear (frequency-independent) contributions $\underset{\sim}{C}_{\text{lin}}$ and the linearized quantities $\underset{\sim}{C}_{\text{nonlin}}$ defined as

$$\underset{\sim}{C}_{\text{lin}} = \begin{bmatrix} c_{\text{bound}} + c_i & -c_i & 0 \\ -c_i & c_i & 0 \\ 0 & 0 & c_s \end{bmatrix}$$

$$\underset{\sim}{C}_{\text{nonlin}} = \begin{bmatrix} r_{EP}(\omega) + r_{I/O}(\omega) & -r_{EP}(\omega) - r_{I/O}(\omega) & 0 \\ -r_{EP}(\omega) - r_{I/O}(\omega) & r_{\text{diss}}(\omega) + r_{EP}(\omega) + r_{I/O}(\omega) & 0 \\ 0 & 0 & 0 \end{bmatrix} \tag{18}$$

where $r_{\text{diss}}(\omega)$, $r_{EP}(\omega)$ and $r_{I/O}(\omega)$, respectively, are the frequency dependent equivalent damping factors of the forces F_{diss}, F_{EP} and $F_{I/O}$, respectively. These factors are shown in Fig. 10 over the frequency range (considering $f = \omega/2\pi$) for different input amplitudes. As can be seen in the left graph, the magnitude of r_{diss} decreases with increasing the amplitude as the friction contribution becomes less important. In contrast, for r_{EP} and $r_{I/O}$, the larger the input force, the greater the equivalent damping factors. Comparing the numerical values for the three damping factors, it can be concluded that the friction of the piston is the most pronounced source of nonlinearity.

In this way, the FID and CS mechanical models of Fig. 4 can be redrawn as in Fig. 11, where the connecting element C_s is the same as in Fig. 4 and f_{diss}, c_{EP} and $c_{I/O}$ are replaced by their linear equivalents.

Comparing the receptance magnitudes of both the nonlinear and the linearized FID in Fig. 12 for a wide range of force amplitudes, the latter approaches almost perfectly the device including nonlinear effects in the entire frequency range considered and for different amplitudes, demonstrating the reliability of the linearization method. Equally, in Fig. 13 the receptances of the nonlinear and the linearized CS are set in contrast. Here again, results show a remarkable match between the two systems. In this case, the agreement is excellent even for low frequencies.
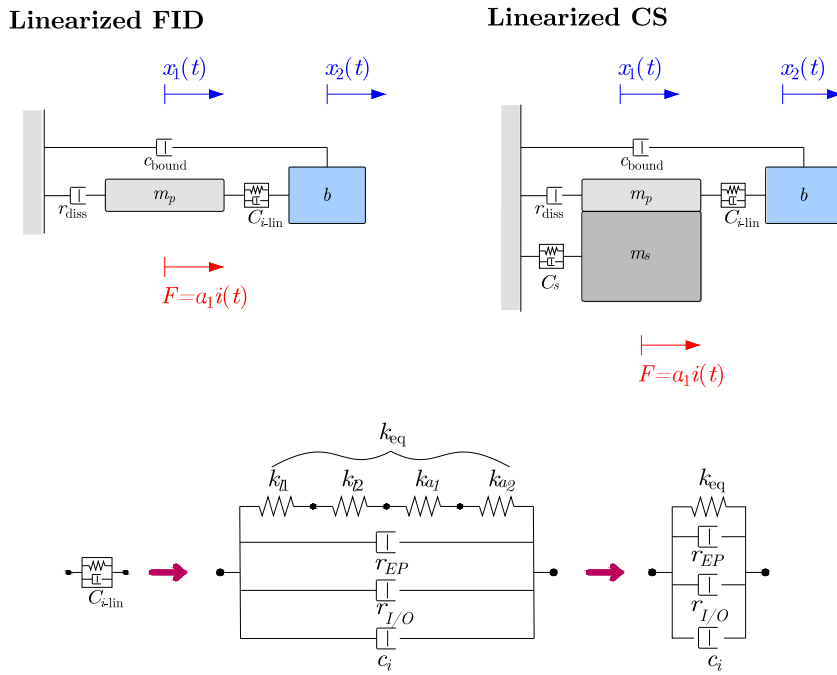
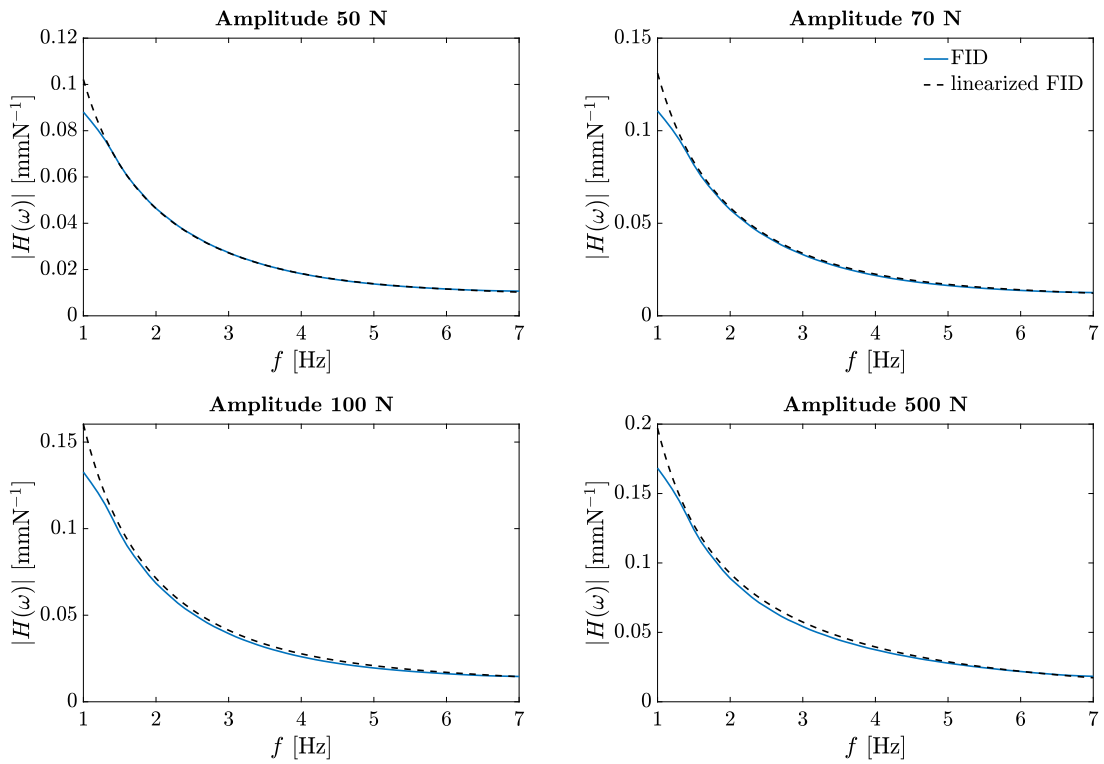**Fig. 11.** Mechanical models of the linearized fluid inerter device (linearized FID) and control system (linearized CS).

Fig. 12. Fluid inerter device (solid blue line) versus linearized fluid inerter device (dashed black line) receptance response.
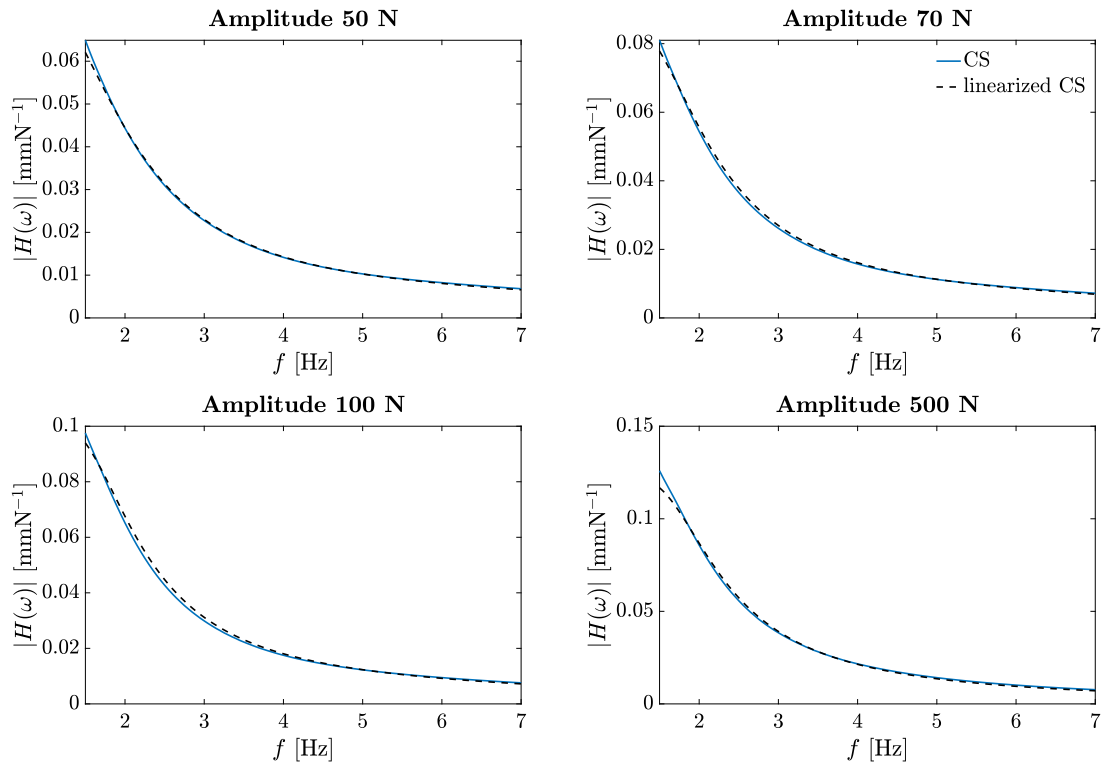
Fig. 13. Controlled system (solid blue line) versus linearized controlled system (dashed black line) receptance response.

5. Finite element model

As mentioned in Section 3, the mechanical model of the FID includes contributions that account for the presence of air in the system. Specifically, the test found that the volume of air increases with increasing excitation intensity, suggesting that cavitation occurs due to changes in pressure of the working fluid. In this study, for the first time a finite element (FE) model of a fluid inerter is created in the commercial software package ABAQUS to investigate the possible consequences that air trapped in the system may cause.

5.1. Numerical method

Considering the problem of a solid cylinder moving in region filled with liquid, the coupled Eulerian–Lagrangian (CEL) method would be a suitable numerical scheme. Here, a Lagrangian kinematic formulation is used for the solid part, where the FE mesh moves with the material, while the motion of the fluid is captured by an Eulerian (spatial) mesh. However, since this type of analysis is available in ABAQUS only with explicit time integration [47] without the possibility of mass scaling, the experimentally observed time period of 60 s would yield a prohibitively large number of time increments in the numerical simulations, since the critical time increment for a reasonably fine mesh is in the order of $\Delta t \approx 10^{-8}$ s.

Assuming the displacements of the piston rod in the cylinder are negligibly small, a coupled acoustic-structural analysis can be performed as alternative to the CEL. In this case, the piston is discretized by Lagrangian solid elements, while the fluid part, consisting of water and air, is discretized with acoustic elements. For the latter, the compressible acoustic wave equation is solved for infinitesimally small fluid particle vibrations, where the energy dissipation in the fluid can be introduced by means of a viscous damping parameter called volumetric drag [47], which is a viscous damper coefficient per unit volume. Although the assumption of small vibrations is clearly not satisfied by the actual inerter, coupled acoustic-structural analyses are conducted here. More specifically, direct-solution steady state simulations are performed, i.e. the system of equations for the discretized model is solved assuming time-harmonic excitation forces.

5.2. Model

For symmetry, a half model of the inerter is created, as depicted in Fig. 14, with the solid and acoustic regions highlighted. Note that a small fraction of the fluid region adjacent to the piston is assumed to be occupied by air, which is varied in the subsequent simulations. While for Young's modulus, Poisson ratio, and mass density of steel are used for the piston, the mass density ρ and
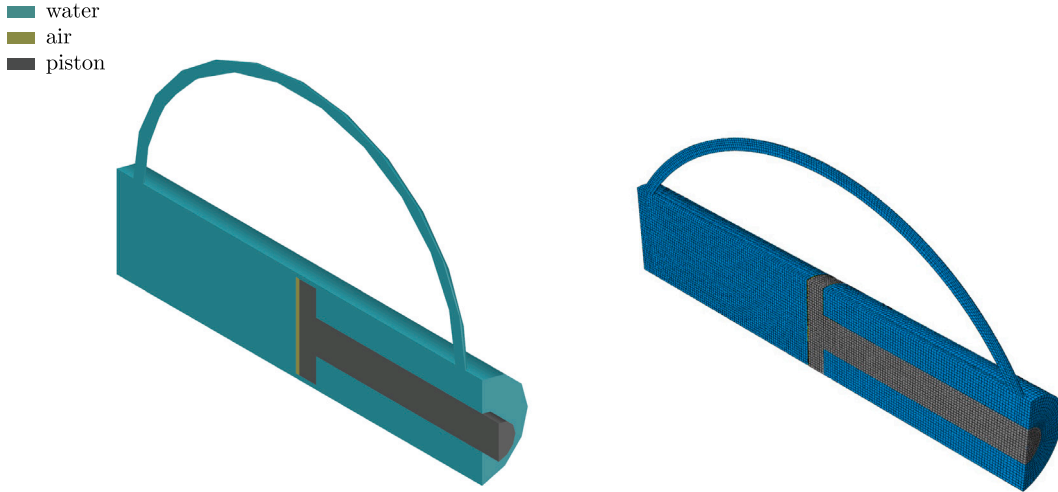
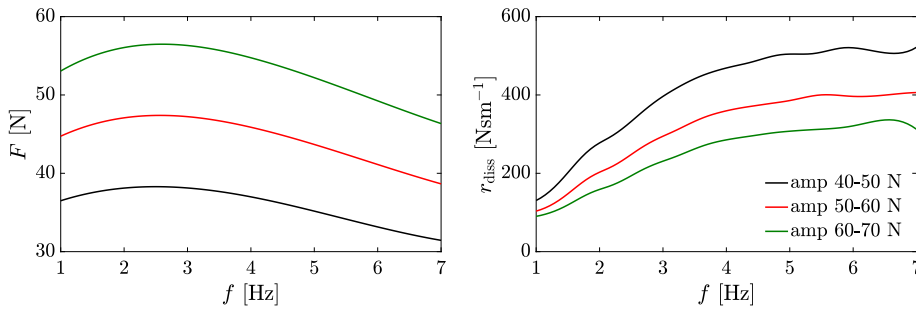**Fig. 14.** CAD (on the left) and FE (on the right) model of the fluid inerter device.

Fig. 15. Force input (on the left) and equivalent dissipation force (on the right) for different input amplitudes.

the bulk modulus B, which can be deduced from the speed of sound, as well as the volumetric drag mentioned above, must be set for the acoustic media. Specifically, for the water, the density ρ_l and bulk modulus B_l are those reported in Table 2, while the volumetric drag coefficient γ_l is assumed to be frequency dependent and its value linearly increases from 5×10^4 N s m^{-4} at 0 Hz to 1.2×10^5 N s m^{-4} at 7 Hz. Similarly, the bulk modulus B_a, density ρ_a and volumetric drag coefficient γ_a of the air are 135296 Pa, 1.293 kg m^{-3} and 10 N s m^{-4}, respectively.

The surface of the piston at the boundary of the FE model is kinematically coupled to a single node on the central axis (not visible in Fig. 14) to facilitate the application of the excitation force. To approximate the experimentally investigated system as close as possible, half of the quantity m_a is added as lumped mass at this node. Also, a connector element to the ground is introduced in which the frequency-dependent equivalent damping coefficient $r_{\text{diss}}(\omega)$ is considered, obtained by linearization as described in the previous section. However, in the contrast to Section 4, the complete electro-mechanical system is considered for linearization. Therefore, the excitation force is no longer constant, but is obtained as $F(t) = \alpha_1 i(t)$ in terms of the electric current in the electro-mechanical system. From these time-histories, envelopes are computed that define the frequency-dependent excitation force for the steady-state simulations corresponding to three different experimentally investigated input amplitudes. The obtained frequency-dependent input force and damping coefficients are shown in Fig. 15 and implemented in the FE model as tabular data.

5.3. Results

In order to obtain a more detailed and physics-based investigation with respect of the amount of air in the system, two sets of tests are performed on the model presented in the previous section. In a first step (test 1), the system is tested with a considerable small amount of air inside (Table 4 - test 1) for the three different amplitudes considered in the experimental setup of the FID. In test 1, the amount od air is assumed to be constant for all the different excitation amplitudes and only the equivalent linear damping of the piston rod r_{diss} is adjusted (Fig. 15.) Subsequently, in order to simulate the formation of air bubbles due to cavitation, the same tests are performed with an increasing amount of air for each amplitude (Table 4 - test 2). Since the input amplitude ranges 40–50 N, 50–60 N and 60–70 N were used successively in the experimental campaign, the air volume due to cavitation is assumed to increase in the same order.

Table 4
Air length setup for the FE simulations.

	Amplitude		40–50 N	50–60 N	60–70 N
Test 1	l_{air} [m]		5×10^{-4}	5×10^{-4}	5×10^{-4}
	V_{air} [m³]		4.9×10^{-7}	4.9×10^{-7}	4.9×10^{-7}
Test 2	l_{air} [m]		5×10^{-4}	20×10^{-4}	30×10^{-4}
	V_{air} [m³]		4.9×10^{-7}	1.96×10^{-6}	2.95×10^{-6}
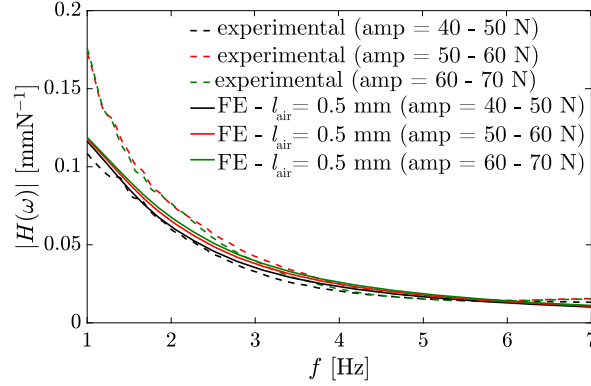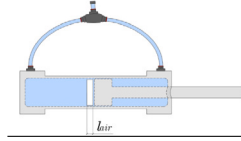
Fig. 16. Test 1: Experimental (dashed lines) vs. FE (solid lines) receptance response for different amplitudes (black: 40–50 N, red: 50–60 N, green: 60–70 N). (For interpretation of the references to color in this figure legend, the reader is referred to the web version of this article.)

Fig. 16 shows the comparison between experimental and FE receptance magnitudes for the different input amplitudes obtained when performing test 1. As can be seen, the outcomes from the FE simulations predict almost the same results for a constant volume of air trapped in the device. In particular, the pronounced nonlinear behavior, especially in the frequency range between 1 and 3 Hz, is not captured.

On the other hand, if the amount of air is adjusted between simulations according to test 2 in Table 4, the numerically and experimentally obtained receptances, shown individually in Fig. 17, match almost perfectly. Therefore, it can be concluded from these FE simulations that the nonlinear behavior in the low-frequency range is dominated by the presence of air inside the system.

6. Conclusions

In this paper, a fluid inerter was studied experimentally in order to assess its vibration control performance. The prototype of such a device consists of a piston-cylinder equipped with an external tube in which the inertia effect was achieved by the convection of a working fluid from the cylinder to the outer tube. Four different configurations, i.e. uncontrolled system, dry inerter device, fluid inerter device and controlled system, were tested in order to properly identify the proposed mechanical models. The systems were investigated in a frequency range between 1 and 10 Hz, performing sine-sweep excitation with different input amplitudes. Three sources of nonlinearity due to dissipative effects and friction were discovered for the fluid inerter device. The derived mechanical models were able to reproduce the experimental results for all tested configurations. The identified nonlinearities were linearized according to energy considerations in order to obtain an equivalent linear system suitable for further parametric studies. Finally, a finite element model of the fluid inerter device was created and the influence of the air trapped in the system was analyzed.

In summary, the following conclusions can be drawn:

- As a further proof of the findings obtained in previous studies, despite the different geometrical design employed here, the theoretically calculated inertance of about 29 kg was generated by the device using only 300 g of flowing fluid. Nevertheless, its tribological and hydraulic nonlinearities are intrinsic properties of the system and cannot be neglected.
- The nonlinear mechanical model developed in this work was able to accurately embody the behavior of a real fluid inerter used to mitigate the vibrations of a single degree of freedom system. Therefore, such a model is suitable for implementing more realistic numerical simulations of control devices whose performance is improved by inerters (Tuned Inerter Dampers, Tuned Mass Damper Inerter, etc.).
- The linearization of the nonlinear mechanical model can be employed for even more extended parametric studies on control systems involving fluid inerters. In addition, appropriate values of the dynamic components of a real inerter can be addressed to alternative optimization methods other than those adapted to the ideal linear case.
- Thanks to the finite element model of the fluid inerter, it has been demonstrated that during experimental testing an increasing amount of air due to cavitation affects the displacement response, especially at low frequencies.
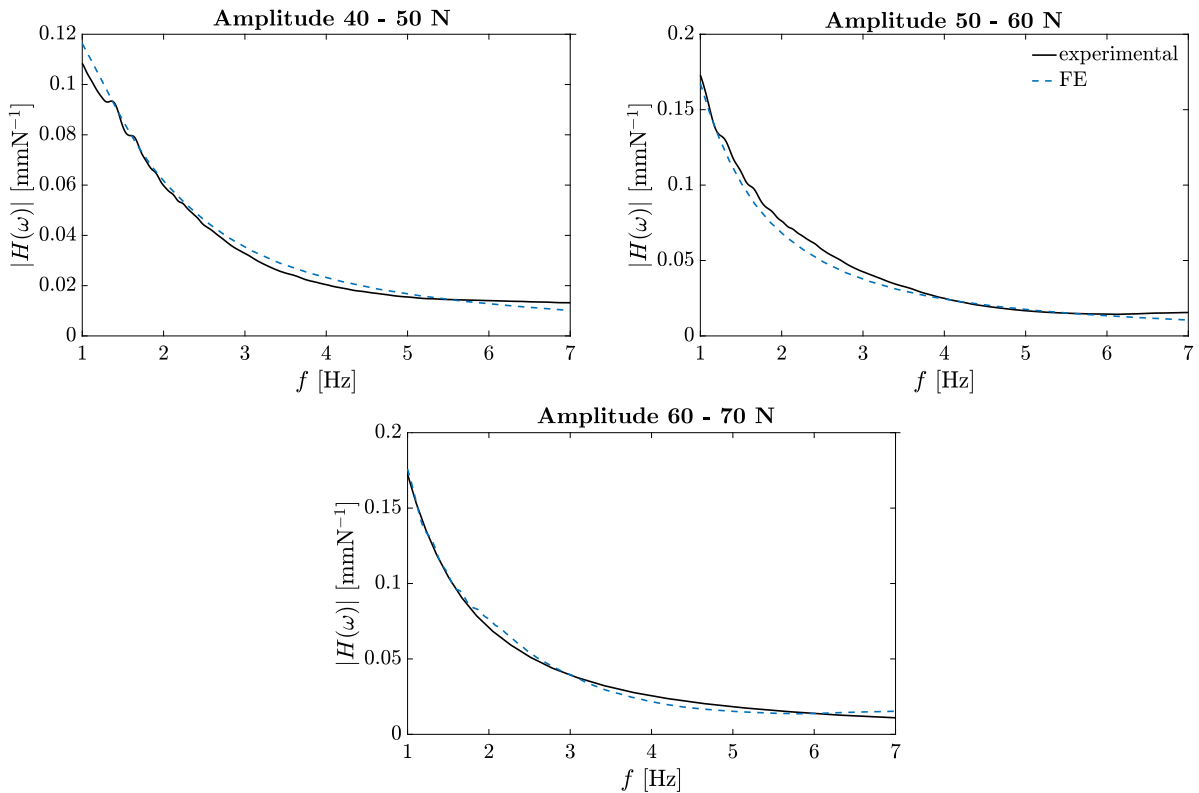
Fig. 17. Test 2: Experimental (solid black lines) vs. FE (dashed blue lines) receptance response for different amplitudes.

Future developments may include the exploitation of the fluid inerter in a large-scale experimental model to analyze possible scaling effects. It is expected that nonlinearities as well as cavitation issues and formation of air bubbles may still occur, however not necessarily proportional to the size of the test rig setup. In addition, further analyses on the finite element model can be implemented to deepen the investigation regarding the influence of the air in the system.

CRediT authorship contribution statement

Miriam Chillemi: Conception and design of study, Acquisition of data, Analysis and/or interpretation of data, Writing – original draft, Writing – review & editing. **Thomas Furtmüller:** Conception and design of study, Acquisition of data, Analysis and/or interpretation of data, Writing – original draft, Writing – review & editing. **Christoph Adam:** Conception and design of study, Writing – original draft, Writing – review & editing. **Antonina Pirrotta:** Writing – review & editing.

Declaration of competing interest

The authors declare that they have no known competing financial interests or personal relationships that could have appeared to influence the work reported in this paper.

Data availability

The data that has been used is confidential.

Acknowledgments

References

[1] M. Smith, Synthesis of mechanical networks: the inerter, IEEE Trans. Automat. Control 47 (10) (2002) 1648–1662, http://dx.doi.org/10.1109/TAC.2002.803532.

[2] F.-C. Wang, W.-J. Su, Impact of inerter nonlinearities on vehicle suspension control, Veh. Syst. Dyn. 46 (7) (2008) 575–595, http://dx.doi.org/10.1080/00423110701519031.

[3] O. Altay, Vibration Mitigation Systems in Structural Engineering, 2021, http://dx.doi.org/10.1201/9781315122243.

[4] J.P. Den Hartog, Mechanical Vibrations, Courier Corporation, 1985.

[5] T. Furtmüller, G. Joas, C. Adam, Control of pendulum oscillations by tuned liquid dampers, J. Fluids Struct. 114 (2022) 103753, http://dx.doi.org/10.1016/j.jfluidstructs.2022.103753.

[6] F. Ziegler, M. Reiterer, Control of vibration prone bridges by tuned liquid column dampers (TLCD), in: 12th International Congress on Sound and Vibration 2005, ICSV 2005, vol. 6, 2005, pp. 5112–5119.

[7] J.M. Kelly, Base isolation: Linear theory and design, Earthq. Spectr. 6 (2) (1990) 223–244, http://dx.doi.org/10.1193/1.1585566.

[8] I. Lazar, S. Neild, D. Wagg, Using an inerter-based device for structural vibration suppression, Earthq. Eng. Struct. Dyn. 43 (8) (2014) 1129–1147, http://dx.doi.org/10.1002/eqe.2390.

[9] F. Petrini, A. Giaralis, Z. Wang, Optimal tuned mass-damper-inerter (TMDI) design in wind-excited tall buildings for occupants' comfort serviceability performance and energy harvesting, Eng. Struct. 204 (2020) 109904, http://dx.doi.org/10.1016/j.engstruct.2019.109904, URL https://www.sciencedirect.com/science/article/pii/S0141029619310983.

[10] C. Masnata, A. Di Matteo, C. Adam, A. Pirrotta, Assessment of the tuned mass damper inerter for seismic response control of base-isolated structures, Struct. Control Health Monit. 28 (2) (2021) e2665, http://dx.doi.org/10.1002/stc.2665.

[11] A. Di Matteo, C. Masnata, C. Adam, A. Pirrotta, Optimal design of tuned liquid column damper inerter for vibration control, Mech. Syst. Signal Process. 167 (2022) 108553, http://dx.doi.org/10.1016/j.ymssp.2021.108553.

[12] K. Ikago, K. Saito, N. Inoue, Seismic control of single-degree-of-freedom structure using tuned viscous mass damper, Earthq. Eng. Struct. Dyn. 41 (3) (2012) 453–474, http://dx.doi.org/10.1002/eqe.1138.

[13] Z. Zhang, T.G. Larsen, Optimal calibration of the rotational inertia double tuned mass damper (RIDTMD) for rotating wind turbine blades, J. Sound Vib. 493 (2021) 115827, http://dx.doi.org/10.1016/j.jsv.2020.115827, URL https://www.sciencedirect.com/science/article/pii/S0022460X20306568.

[14] R. Ma, K. Bi, H. Hao, Inerter-based structural vibration control: A state-of-the-art review, Eng. Struct. 243 (2021) 112655, http://dx.doi.org/10.1016/j.engstruct.2021.112655, URL https://www.sciencedirect.com/science/article/pii/S0141029621008051.

[15] M. Chillemi, T. Furtmüller, C. Adam, A. Pirrotta, Assessing the effect of different configurations of inerter-based devices for structural vibration control, in: 16th International Conference on Dynamical Systems. Theory and Applications, vol. 2, 2021, pp. 205–206.

[16] M.C. Smith, Force-controlling mechanical device, 2002, U.S. Patent 7, 316, 303 B2.

[17] F.-C. Wang, M.-S. Hsu, W.-J. Su, T.-C. Lin, Damping and inertial hydraulic device, 2009, U.S. Patent 2009/0108510 A1.

[18] C. Papageorgiou, N. Houghton, M. Smith, Experimental testing and analysis of inerter devices, J. Dyn. Syst. Meas. Control-Trans. Asme - J DYN SYST MEAS CONTR 131 (2009) http://dx.doi.org/10.1115/1.3023120.

[19] B.J. Gartner, M.C. Smith, Damping and inertial hydraulic device, 2011, U.S. Patent 13/577, 234.

[20] S. Sarkar, B. Fitzgerald, Fluid inerter for optimal vibration control of floating offshore wind turbine towers, Eng. Struct. 266 (2022) 114558, http://dx.doi.org/10.1016/j.engstruct.2022.114558.

[21] R. Tuluie, Fluid inerter, 2010, U.S. Patent 13/575, 017.

[22] A. Gonzalez-Buelga, I.F. Lazar, J.Z. Jiang, S.A. Neild, D.J. Inman, Assessing the effect of nonlinearities on the performance of a tuned inerter damper, Struct. Control Health Monit. 24 (3) (2017) e1879, http://dx.doi.org/10.1002/stc.1879.

[23] M.Z.Q. Chen, M.C. Smith, Restricted complexity network realizations for passive mechanical control, IEEE Trans. Automat. Control 54 (10) (2009) 2290–2301, http://dx.doi.org/10.1109/TAC.2009.2028953.

[24] E. John, D. Wagg, Design and testing of a frictionless mechanical inerter device using living-hinges, J. Franklin Inst. B 356 (14) (2019) 7650–7668, http://dx.doi.org/10.1016/j.jfranklin.2019.01.036.

[25] P. Brzeski, M. Lazarek, P. Perlikowski, Experimental study of the novel tuned mass damper with inerter which enables changes of inertance, J. Sound Vib. 404 (2017) 47–57, http://dx.doi.org/10.1016/j.jsv.2017.05.034, URL https://www.sciencedirect.com/science/article/pii/S0022460X17304236.

[26] L. Yuehao, C. Zhe, H. Niaoqing, Y. Yi, X. Zhuo, Modeling, design and experiments of a ball-screw inerter with mechanical diodes, J. Sound Vib. 504 (2021) 116121, http://dx.doi.org/10.1016/j.jsv.2021.116121.

[27] M.C. Smith, The inerter: A retrospective, Ann. Rev. Control Robot. Auton. Syst. 3 (1) (2020) 361–391, http://dx.doi.org/10.1146/annurev-control-053018-023917.

[28] F.-C. Wang, M.-R. Hsieh, H.-J. Chen, Stability and performance analysis of a full-train system with inerters, Veh. Syst. Dyn. 50 (4) (2012) 545–571, http://dx.doi.org/10.1080/00423114.2011.606368.

[29] M.Z. Chen, Y. Hu, Inerter and Its Application in Vibration Control Systems, Springer, 2019.

[30] C. Liu, L. Chen, H.P. Lee, Y. Yang, X. Zhang, A review of the inerter and inerter-based vibration isolation: Theory, devices, and applications, J. Franklin Inst. B 359 (14) (2022) 7677–7707, http://dx.doi.org/10.1016/j.jfranklin.2022.07.030, URL https://www.sciencedirect.com/science/article/pii/S0016003222005129.

[31] Z. Li, K. Xu, K. Bi, Q. Han, X. Du, Inerter nonlinearity and its influence on control efficiency of tmdi for suppressing vortex-induced vibration of bridges, J. Bridge Eng. 27 (11) (2022) 04022101, http://dx.doi.org/10.1061/(ASCE)BE.1943-5592.0001941.

[32] K. Madhamshetty, J. Manimala, Low-rate characterization of a mechanical inerter, Machines 6 (2018) 32, http://dx.doi.org/10.3390/machines6030032.

[33] D. De Domenico, G. Ricciardi, R. Zhang, Optimal design and seismic performance of tuned fluid inerter applied to structures with friction pendulum isolators, Soil Dyn. Earthq. Eng. 132 (2020) 106099, http://dx.doi.org/10.1016/j.soildyn.2020.106099.

[34] Y. Shen, L. Chen, Y. Liu, X. Zhang, X. Yang, Optimized modeling and experiment test of a fluid inerter, J. Vibroeng. 18 (5) (2016) 2789–2800, http://dx.doi.org/10.21595/jve.2016.16885.

[35] M. Chillemi, T. Furtmüller, C. Adam, A. Pirrotta, Nonlinear mechanical model of a fluid inerter, Mech. Syst. Signal Process. 188 (2023) 109986, http://dx.doi.org/10.1016/j.ymssp.2022.109986.

[36] C. Liu, L. Chen, X. Zhang, Y. Yang, J. Nie, Design and tests of a controllable inerter with fluid-air mixture condition, IEEE Access 8 (2020) 125620–125629, http://dx.doi.org/10.1109/ACCESS.2020.3007918.

[37] S.J. Swift, M.C. Smith, A.R. Glover, C. Papageorgiou, B. Gartner, N.E. Houghton, Design and modelling of a fluid inerter, Internat. J. Control 86 (11) (2013) 2035–2051, http://dx.doi.org/10.1080/00207179.2013.842263.

[38] J.S. S. Jaiswal, A. Mikkola, Efficiency comparison of various friction models of a hydraulic cylinder in the framework of multibody system dynamics, Nonlinear Dynam. 104 (4) (2021) 3497–3515, http://dx.doi.org/10.1007/s11071-021-06526-9.

[39] G.F. Lang, D. Snyder, et al., Understanding the physics of electrodynamic shaker performance, Sound Vib. 35 (10) (2001) 24–33.

[40] A. Zangwill, Modern Electrodynamics, Cambridge University Press, 2012, http://dx.doi.org/10.1017/CBO9781139034777.

[41] T. Furtmüller, A. Di Matteo, C. Adam, A. Pirrotta, Base-isolated structure equipped with tuned liquid column damper: An experimental study, Mech. Syst. Signal Process. 116 (2019) 816–831, http://dx.doi.org/10.1016/j.ymssp.2018.06.048.

[42] Li Chun Bo, D. Pavelescu, The friction-speed relation and its influence on the critical velocity of stick-slip motion, Wear 82 (3) (1982) 277–289, http://dx.doi.org/10.1016/0043-1648(82)90223-X.

[43] P. Brown, J. McPhee, A continuous velocity-based friction model for dynamics and control with physically meaningful parameters, J. Comput. Nonlinear Dyn. 11 (5) (2016) http://dx.doi.org/10.1115/1.4033658.

[44] S. Bhattacharyya, A.D. Ghosh, B. Basu, Nonlinear modeling and validation of air spring effects in a sealed tuned liquid column damper for structural control, J. Sound Vib. 410 (2017) 269–286, http://dx.doi.org/10.1016/j.jsv.2017.07.046.

[45] W. Jiang, X. Luo, X. Chen, Influence of structural flexibility on the nonlinear stiffness of hydraulic system, Adv. Mech. Eng. 8 (2016) http://dx.doi.org/10.1177/1687814016663806.

[46] M. Richardson, R. Potter, Viscous vs. structural damping in modal analysis, in: 46th Shock and Vibration Symposium, Vol. 175, Citeseer, 1975.

[47] A.S.U. Manual, Abaqus 6.11, http://130.149 89 (2080) (2012) v6.